Optically Abrupt Localized Surface Plasmon Resonances in Si Nanowires by Mitigation of Carrier Density Gradients

Li-Wei Chou,† Dmitriy S. Boyuk,† and Michael A. Filler*

School of Chemical & Biomolecular Engineering, Georgia Institute of Technology, Atlanta, Georgia 30332, United States. †These authors contributed equally to this work.

ABSTRACT Spatial control of carrier density is critical for engineering and exploring the interactions of localized surface plasmon resonances (LSPRs) in nanoscale semiconductors. Here, we couple *in situ* infrared spectral response measurements and discrete dipole approximation (DDA) calculations to show the impact of axially graded carrier density profiles on the optical properties of mid-infrared LSPRs supported by Si nanowires synthesized by the vapor–liquid–solid technique. The region immediately adjacent to each intentionally encoded resonator (*i.e.*, doped segment) can exhibit residual carrier densities as high as 10^{20} cm^{-3}, which strongly modifies both near- and far-field behavior. Lowering substrate temperature during the spacer segment growth reduces this residual carrier density and results in a spectral response that is indistinguishable from nanowires with ideal, atomically abrupt carrier density profiles. Our experiments have important implications for the control of near-field plasmonic phenomena in semiconductor nanowires, and demonstrate methods for determining and controlling axial dopant profile in these systems.

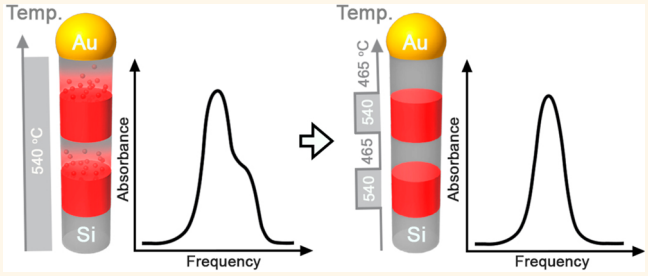

KEYWORDS: silicon · nanowire · doping profile · surface plasmon resonance

Plasmonics offers a route to confine electromagnetic waves into deep-subwavelength volumes. While conventional metals are traditionally leveraged for this purpose,[1–3] semiconductors are now receiving increased attention.[4–6] Unlike the fixed carrier densities of metals, semiconductors enable modulation of charge carrier density *via* chemical doping, electrostatic gating, and/or optical excitation.[7] This capability opens the door to tuning localized surface plasmon resonance (LSPR) frequency and absorption strength, with new opportunities in applications such as photothermal therapy,[8] smart windows,[9] chemical sensing,[10] and information processing.[11,12] Si-based materials offer the additional advantages of elemental abundance and extensive processing know-how.

Robust control of carrier density profile is critical for harnessing the near-field effects extensively studied for metal nanoparticles,[13–16] and which serve as the basis of ultrasensitive spectroscopy,[17] compact waveguides,[2] nonlinear optical enhancements,[18] and even catalysis.[19] When two LSPR-supporting nanoparticles are brought into close proximity, tremendous local electric field enhancements are generated between them. The strength of such near-field interactions, and thus the magnitude of the local field enhancement, inversely depends on interparticle separation (above the quantum regime).[20] Nanoparticle dimensions, and thus interparticle spacing, are easily defined for metals since the carrier density profile is uniform throughout. However, the "dimensions" of a plasmonic semiconductor nanoparticle will also depend on its carrier density profile. Thus, to engineer near-field interactions in plasmonic semiconductor nanoparticles, it is imperative to understand and control the factors governing the placement and activation of dopant atoms.

Vapor–liquid–solid (VLS) synthesis—where a liquid catalyst droplet collects

* Address correspondence to michael.filler@chbe.gatech.edu.

Received for review September 3, 2014 and accepted January 22, 2015.

Published online January 22, 2015
10.1021/nn504974z

atoms from the vapor and directs crystallization of the solid[21−23]—permits the incorporation of multiple, axially registered doped segments, and thus LSPRs, along the length of individual nanowires.[24] This method allows for reasonable control of dopant profile by temporally modulating dopant precursor (*e.g.*, PCl_3 for phosphorus doping of Si nanowires[24]) delivery, but axial gradients are common and limit the plasmonic design space for nanowires.[25] Such behavior is most often explained with the so-called "reservoir effect," where atoms in the finite volume growth catalyst continue to incorporate into the nanowire even after precursor flow ceases.[26−29]

In the present work, we show the impact of axially carrier density gradients on the spectral response of Si nanowires containing multiple resonators. *In situ* infrared spectral response measurements and scattering simulations within the discrete dipole approximation (DDA) are a powerful method to study these effects.[30] A considerable residual carrier density remains in the spacer segment between intentionally encoded resonators that yields unexpected spectral features and modifies near-field interactions. A reduction of substrate temperature during spacer segment growth can mitigate these effects. We use this approach to fabricate Si nanowires with spectral responses indistinguishable from those of nanowires with ideal, atomically abrupt carrier density profiles. In addition to studying the optical properties of doped Si nanowires, our methodology is useful for probing complex carrier density profiles that can be challenging for transport measurements, electron holography, Kelvin force probe microscopy, and scanning photocurrent microscopy.[31−34]

RESULTS AND DISCUSSION

Figure 1a shows a series of experimental spectral response measurements for arrays of Si nanowires containing 0 to 5 "primary" (*i.e.*, intentionally encoded) resonators. Our prior work shows that the carrier density of resonators fabricated in this manner is near 2.3×10^{20} cm^{-3} and that the observed spectral features result from resonant absorption, rather than scattering.[30] Representative SEM images of Si nanowires after buffered HF etching are displayed in the Figure 1a inset and reveal the geometry of each resonator. All aspect ratios appear the same within the limits of this etching technique. As expected, a single absorption band is observed for Si nanowires containing one primary resonator. However, the absorption features for Si nanowires containing 2 to 5 resonators exhibit a pronounced asymmetry consistent with multiple, convoluted peaks.

We simulate the spectral response of the longitudinal LSPR to further understand this behavior. Figure 1b shows calculated absorption efficiencies for Si nanowires with 0−5 primary resonators

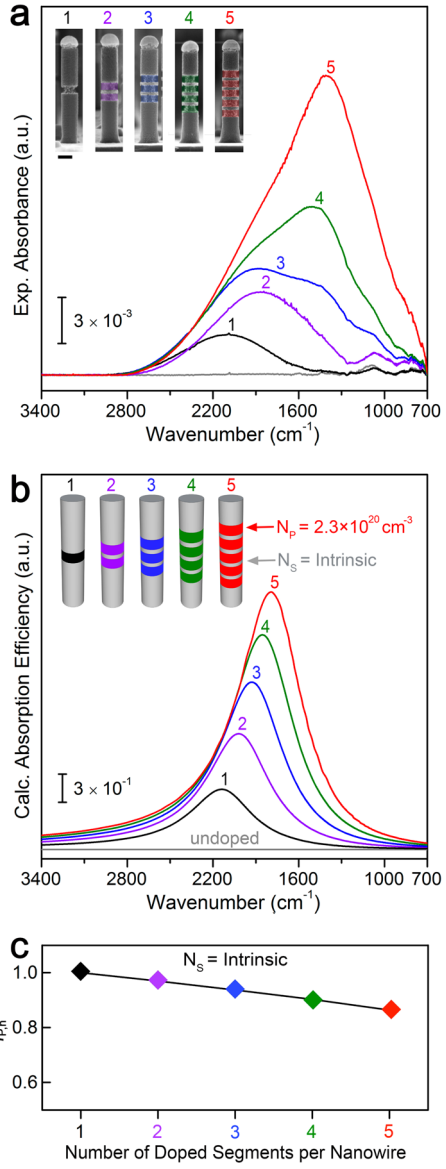

Figure 1. Comparison of experimental and expected Si nanowire spectral responses for the longitudinal LSPR. (a) Experimental spectral response for an array of Si nanowires containing 0−5 primary resonators. Primary resonators and spacer segments are grown at a substrate temperature of 540 °C. Inset: Side view SEM images of representative nanowires following a buffered oxide etch treatment to determine doped segment geometry. (b) Calculated absorption efficiency for individual Si nanowires containing 0−5 primary resonators ($N_P = 2.3 \times 10^{20}$ cm^{-3}) and intrinsic spacer segments (N_S = intrinsic Si). (c) Integrated absorption efficiencies from the spectra in (b) normalized according to eq 1.

($N_P = 2.3 \times 10^{20}$ cm^{-3}) with intrinsic "spacer" segments (N_S = intrinsic). Our simulations predict, consistent with the scattering of metal particles arranged in 1-D chains,[35] a monotonically increasing absorption intensity and redshift of the absorption maximum as the number of primary resonators increases. The substantial redshift observed in Figure 1b ($\Delta\nu_{1-5} = 347$ cm^{-1}) suggests strong near-field coupling for this system, as expected due to the large dielectric constant of

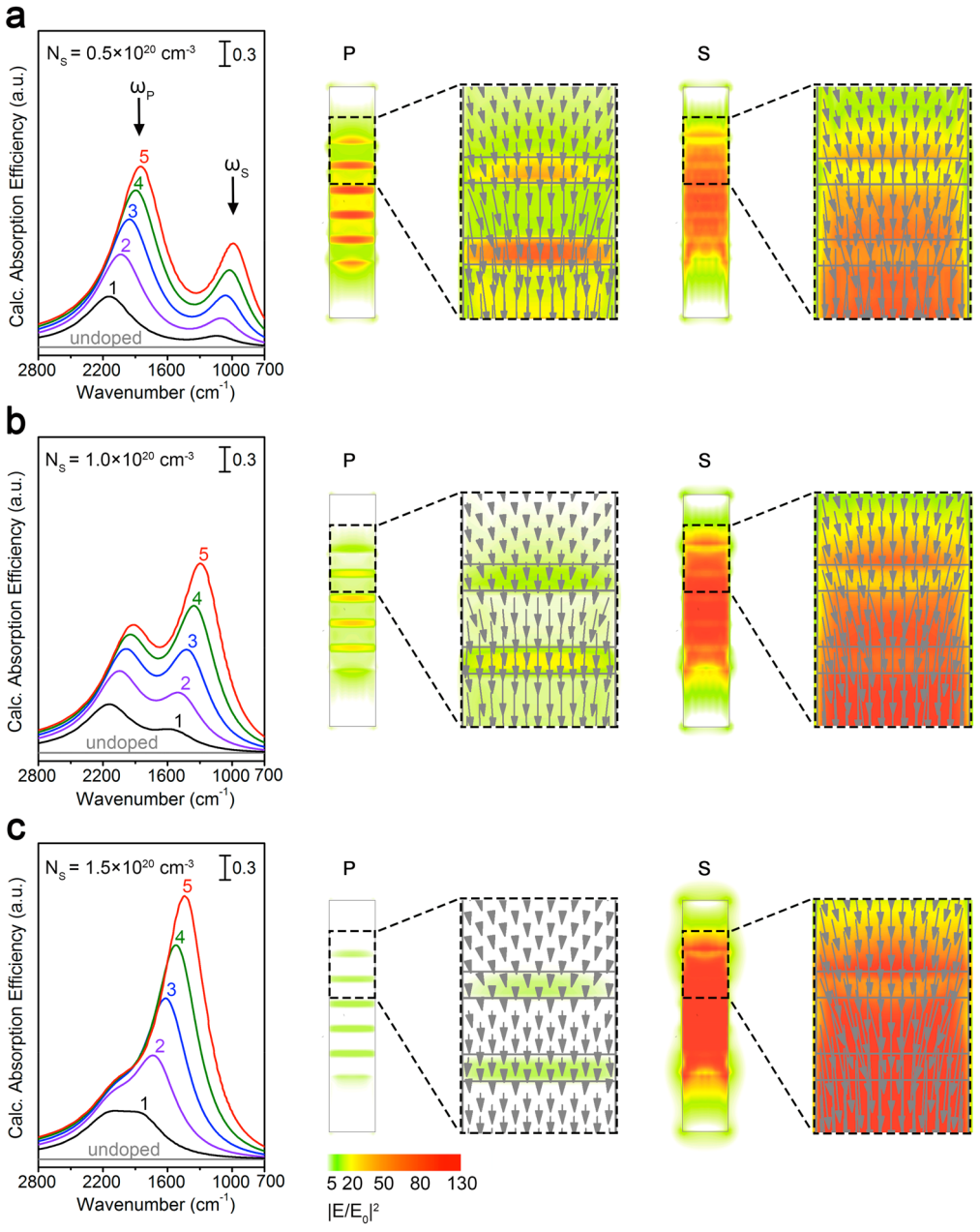

Figure 2. Effect of spacer segment carrier density on longitudinal LSPR. Calculated longitudinal mode absorption efficiencies for individual Si nanowires containing 0−5 primary resonators ($N_P = 2.3 \times 10^{20}$ cm^{-3}) with spacer segments exhibiting carrier densities (N_S) of (a) 0.5, (b) 1.0, and (c) 1.5×10^{20} cm^{-3}. The high (labeled "ω_P") and low (labeled "ω_S") frequency absorption modes are largely attributed to the "primary" and "spacer" segments, respectively. E-field enhancement maps and polarization vector plots of the P and S mode at each value of N_S are shown for the case of 5 primary resonators, and determined at the absorption efficiency maximum of each mode. The magnitude of the E-field enhancement is indicated by a green-to-red gradient.

intrinsic Si and anisotropic dielectric environment of the nanowire geometry.[30] The effect of adding an additional resonator can be quantified, as shown in Figure 1c, by normalizing the integrated absorption efficiency according to eq 1:

$$\hat{I}_{j,n} = \frac{I_{j,n}}{I_{j,1}n} \quad (1)$$

where $I_{j,n}$ and $\hat{I}_{j,n}$ are the measured and normalized integrated intensity of the jth mode for nanowires with n primary resonators, respectively. While there is only one mode in Figure 1b, and thus no need to distinguish between multiple modes, this definition is useful for the subsequent discussion. Notably, Figure 1c shows that each additional resonator (1−5) provides an increasingly smaller absorption enhancement, despite adding the same number of additional charge carriers. We attribute this behavior to the proximity of the doped segments, where a neighboring segment acts to lower the overall dielectric function of the

surroundings. A constant increase in absorption enhancement would be expected for doped segments with larger spacing. The simulated spectral response for the transverse LSPR (Supporting Information, Figure S1) exhibits additional complexity. However, its contribution to the experimental spectra is negligible, as its absorption efficiency is an order of magnitude lower than that for the longitudinal LSPR. As shown in our previous work, the optical properties of undoped Si and the nanowire's anisotropic dielectric structure produce an image dipole that strongly damps the transverse LSPR.[30] We include these data for the transverse LSPR here and below for completeness.

We hypothesize that the differences observed between Figure 1a and 1b result from dopant profiles in our fabricated Si nanowires that are less abrupt than the ideal profiles used in the simulation. To explore this possibility, we numerically investigate nanowires with primary resonators separated by spacer segments with nonzero carrier densities. Figure 2 displays calculated absorption efficiencies and electric-field enhancement maps for the longitudinal LSPR with 0−5 primary resonators (N_P = 2.3 × 10^{20} cm^{-3}) and N_S values of 0.5, 1.0, and 1.5 × 10^{20} cm^{-3}. Two distinct absorption features are present in all cases. The high (labeled "ω_P") and low (labeled "ω_S") energy modes result from absorption predominantly arising from the primary resonators and spacer segments, respectively. Both modes redshift and increase in intensity as the number of resonators increases. The frequency and absorption strength of the S mode also increases concomitantly with spacer segment carrier density. The transverse LSPR remains weak for any number of primary resonators (Supporting Information, Figure S2).

The complex dielectric structure of the doping superlattices contained in these nanowires also leads to other, less obvious behavior. Figure 3 displays the normalized integrated intensity of each mode (*i.e.*, P and S) as per eq 1. Analogous to that observed for nanowires with intrinsic spacer segments (Figure 1c), Figure 3a indicates that the values of $\hat{I}_{P,n}$ are incrementally smaller with each additional resonator. More importantly, the extent of this effect increases as a function of spacer segment carrier density (N_S). We attribute this behavior to changes in the dielectric function of the spacer segments *at the frequency of the P mode*.[36] For intrinsic spacer segments, the real part of Si's dielectric function, ε_S (where the subscript 'S' denotes the spacer segment), is 11.6 and independent of frequency in the infrared. In this situation, the intrinsic Si strongly polarizes and enhances primary resonator coupling. However, ε_S decreases as N_S increases *at the frequency of the P mode*. For example, ε_S = 5.2 for a spacer segment with a carrier density of 1.0 × 10^{20} cm^{-3} at ω_P = 2139 cm^{-1}. The reduced polarizability of the spacer segment hinders coupling,

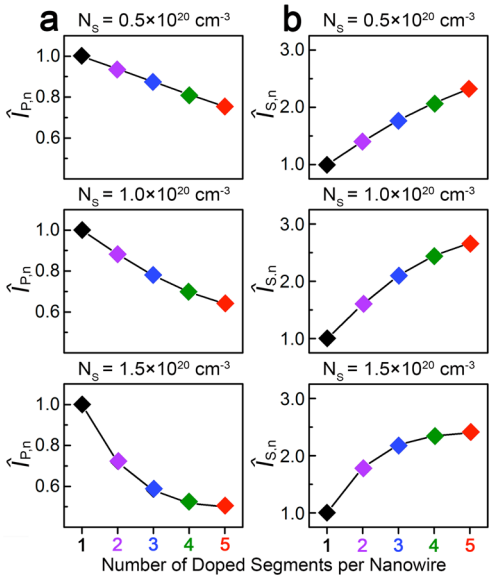

Figure 3. Normalized absorption strength. Integrated absorption efficiencies of the (a) P and (b) S modes from the spectra in Figure 2 normalized according to eq 1 for individual Si nanowires containing 1−5 primary resonators (N_P = 2.3 × 10^{20} cm^{-3}) with spacer segments exhibiting carrier densities (N_S) of 0.5, 1.0, and 1.5 × 10^{20} cm^{-3}.

as seen in the electric-field enhancement maps of Figure 2, and reduces P mode absorption strength. $\hat{I}_{P,n}$ drops most quickly upon adding the first few resonators (*e.g.*, from n = 1 to 2), as most easily seen for N_S = 1.5 × 10^{20} cm^{-3}. This effect stems from the substantial changes in dielectric environment upon transitioning from that of purely intrinsic Si to one that is partially doped. Figure 3b shows that $\hat{I}_{S,n}$ increases as a function of resonator number, indicating enhanced coupling of the spacer segments. This effect is the inverse of that discussed above for the P mode. In other words, ε_P increases *at the frequency of the S mode* as N_S increases.

We next model the spacer segment as two domains with stepped carrier densities to more accurately capture the behavior seen in our experiments. Figure 4 displays simulations of absorption efficiency for Si nanowires with 0−5 primary resonators (N_P = 2.3 × 10^{20} cm^{-3}) separated by two 10 nm spacer segments (20 nm total) with carrier densities of N_{S1} = 1.5 × 10^{20} cm^{-3} and N_{S2} = 0.5 × 10^{20} cm^{-3}. The trends observed as a function of primary resonator number are consistent with the experimental data in Figure 1a and provide strong evidence that the interfaces between undoped and doped segments exhibit graded carrier densities for our standard growth conditions. We attribute these axial carrier density gradients to the "reservoir effect." As illustrated in Figure 5a, upon terminating dopant precursor flow, the concentration of dopant atoms inside the catalyst (*i.e.*, the reservoir) must be depleted. Recent studies indicate

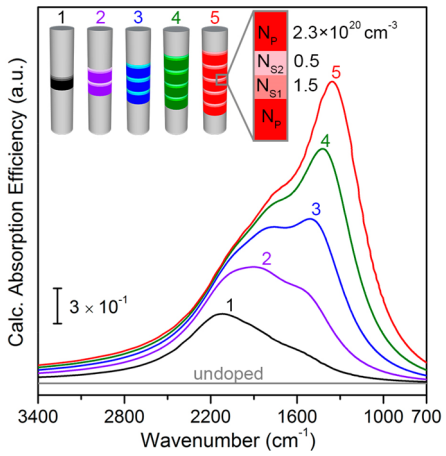

Figure 4. Effect of stepped carrier density profile. Calculated absorption efficiencies for individual Si nanowires containing 0−5 primary resonators (N_P = 2.3 × 10^{20} cm^{-3}) and spacer segments with a two-step carrier density gradient (N_{S1} = 1.5 × 10^{20} cm^{-3}, N_{S2} = 0.5 × 10^{20} cm^{-3}).

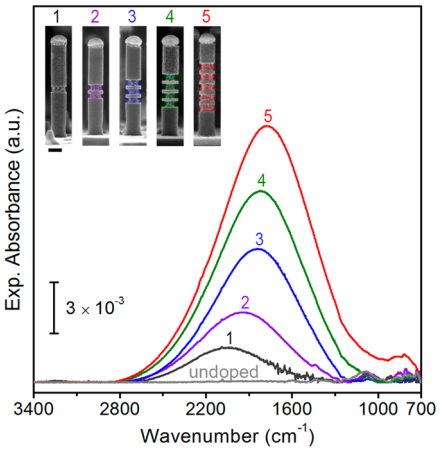

Figure 6. Demonstration of optically abrupt resonators. Experimental spectral response for an array of Si nanowires containing 0−5 primary resonators. Primary resonators and spacer segments are grown at a substrate temperature of 540 and 465 °C, respectively. Inset: Side view SEM images of representative nanowires following a buffered oxide etch treatment to determine doped segment geometry.

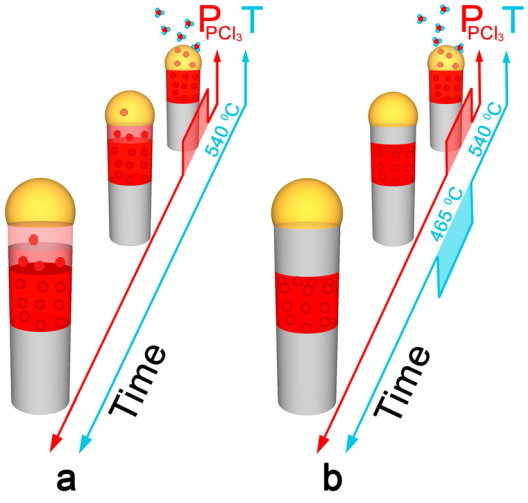

Figure 5. Schematic of single- and two-temperature nanowire growth protocols. (a) At high substrate temperature, phosphorus atoms remaining in the catalyst after termination of PCl_3 flow continue to incorporate into the nanowire. (b) A reduction of substrate temperature during spacer segment growth improves carrier density profile abruptness.

that these concentrations can be quite high (0.3 at. % P in an AuGe eutectic at 380 °C).[37] Residual atoms are incorporated into the nanowire as elongation continues, leading to an axial compositional gradient whose characteristic length is proportional to nanowire diameter and dopant atom concentration in the growth catalyst.[25,26]

A modified growth protocol, where the spacer segment is grown at a lower substrate temperature, minimizes the observed carrier density gradients. As displayed in Figure 5b, we use substrate temperatures of 540 and 465 °C for segment growth with and without PCl_3 flow, respectively. Figure 6 shows that the experimental spectral responses for Si nanowires synthesized in this manner exhibit single peaks that redshift as the number of primary resonators increases. The agreement between these data and our simulations of nanowires with ideal dopant profiles (Figure 1b) indicates a substantial reduction of residual phosphorus in the spacer segment and improvement in profile abruptness. The mechanism by which dopant atoms inside the catalyst (*i.e.*, the reservoir) are depleted is beyond the scope of this work, but may occur *via* accelerated injection into the solid nanowire, ejection onto the nanowire sidewalls,[38] or evaporation to the gas phase.[39] While a residual phosphorus concentration in the spacer segment may still be on the order of 10^{18} cm^{-3}, and undetectable with the current approach, carrier densities below 1 × 10^{19} cm^{-3} do not significantly impact Si's dielectric function in the infrared.[36] Hence, we refer to resonators fabricated using the modulated temperature growth process as "optically abrupt" since the spectral response of these nanowires is indistinguishable from nanowires with ideal carrier density profiles.

CONCLUSION

We characterize the effect of graded carrier densities on the LSPRs of phosphorus-doped Si nanowires with a combination of experimental spectral response measurements and DDA simulations. A reduction of substrate temperature immediately following primary resonator fabrication improves carrier density profile and enables optically abrupt spectral responses. The understanding and control of nanowire doping demonstrated here is particularly important for future applications leveraging near-field interactions, such as optical interconnects and

molecular detection.[3,40] Our findings also suggest control of spacer segment carrier density as a route to dynamically modulate LSPR coupling and spectral response.

MATERIALS AND METHODS

Experimental protocols are similar to our previous work[41,42] and briefly summarized here. A Si(111) substrate (El-Cat, FZ, 15−30 Ω-cm, double side polished) is initially cleaned in HF (J.T. Baker, 10%) for 5 min and rinsed in deionized water prior to insertion into a custom-built ultrahigh vacuum (UHV) chamber. Pressures are not corrected for ion gauge sensitivity. The substrate is resistively annealed at 700 °C for 1 h and then flashed to 1200 °C for 30 s in vacuum. A thin film of Au (ESPI Metals, 99.999%) is thermally evaporated at a rate of 1 nm/min after cooling to room temperature at a rate of approximately 2 °C/s.

Nanowire arrays are grown using the VLS technique in a two-step process. During the "incubation step," which includes Au film break up, Ostwald ripening, and initial nanowire nucleation, the substrate temperature is ramped to and held at 620 °C while maintaining a 4×10^{-5} Torr Si_2H_6 (Voltaix, 99.998%) partial pressure for 5 min. Nanowire array areal densities near 1 nanowire/μm^2 are obtained with this procedure. To initiate the "elongation step," where nanowires are grown and encoded with one or more phosphorus-doped segments, the substrate temperature is lowered to 540 °C at a rate of 3 °C/s at constant Si_2H_6 partial pressure. Phosphorus-doped segments are generated by introducing PCl_3 (Strem Chemicals, 99.999%) at a partial pressure of 3×10^{-6} Torr. Between each doped segment, as described in the main text, the substrate temperature is either maintained at 540 °C or reduced to 465 °C. Nanowire growth rates are approximately 9 and 5 nm/min at 4×10^{-5} Torr Si_2H_6 and substrate temperatures of 540 and 465 °C, respectively. PCl_3 partial pressures as high as 3.0×10^{-6} Torr do not strongly impact nanowire growth rate.[41]

The extinction spectra of as-grown nanowire arrays are measured *in situ* at room temperature using infrared spectroscopy (Bruker, Vertex 70) with a transmission geometry. Unpolarized light from a SiC light source is used in combination with a liquid nitrogen-cooled HgCdTe detector and a KBr beam splitter to collect data between 700 and 3400 cm^{-1} with a resolution of 4 cm^{-1}. All spectra are recorded at an angle of incidence of 58° to probe the longitudinal LSPR absorption mode. As the absorption strength of the transverse LSPR is more than an order of magnitude weaker than the longitudinal LSPR (Supporting Information, Figure S1), the measured spectral response is almost entirely due to the longitudinal LSPR. Spectra are subsequently processed by subtracting those recorded at 0° and baselined with a concave rubberband method. To reveal doped segment geometry, nanowire arrays are etched in buffered HF (J.T. Baker, 5:1) solution for up to 3 min after spectral response measurement and removal from the vacuum system. Nanowire morphology is examined using a Zeiss Ultra-60 field-emission scanning electron microscope (SEM).

Doped Si nanowire spectral response is simulated within the discrete dipole approximation (DDA) using the DDSCAT 7.3 code, analogous to that described previously.[30] The LATTDR method utilized here yields results effectively equivalent to those from GKDLTR and FLTRCD (Supporting Information, Figure S1). The spectral response, local field enhancement, and polarization vector map for a longitudinally applied electric field are calculated for individual, cylindrical nanowires with overall dimensions matching those of as-synthesized nanowires, specifically a length of 650 nm and diameter of 130 nm. Simulations of individual nanowires are appropriate for the present work since inter-nanowire coupling is negligible for arrays with low areal densities (~1 nanowire/μm^2). All "primary" (*i.e.*, intentionally encoded) resonators are modeled with carrier densities, N_P, of 2.3×10^{20} cm^{-3} and lengths of 50 nm. Each primary resonator is separated by a 20 nm spacer region. The carrier density of the "spacer" region, N_S, is varied as described in the main text. Each nanowire is simulated using a total of 8905 dipoles with a periodic grid spacing of 10 nm. The refractive indices (n) and extinction coefficients (k) of bulk Si as a function of carrier density are obtained from Palik and an extended Drude model.[36] A conjugate gradient iteration is applied until the error tolerance is below 10^{-5}. Lorentzian peak fits are completed with Origin 9.0.

Conflict of Interest: The authors declare no competing financial interest.

Supporting Information Available: Comparison of DDA method and longitudinal *vs* transverse LSPRs; effect of spacer segment carrier density on transverse LSPR. This material is available free of charge *via* the Internet at http://pubs.acs.org.

Acknowledgment. The authors gratefully acknowledge support from the Camille and Henry Dreyfus Postdoctoral Program in Environmental Chemistry and National Science Foundation IGERT program.

REFERENCES AND NOTES

1. Link, S.; El-Sayed, M. A. Shape and Size Dependence of Radiative, Non-Radiative and Photothermal Properties of Gold Nanocrystals. *Int. Rev. Phys. Chem.* **2000**, *19*, 409–453.
2. Maier, S. A.; Atwater, H. A. Plasmonics: Localization and Guiding of Electromagnetic Energy in Metal/Dielectric Structures. *J. Appl. Phys.* **2005**, *98*, 011101.
3. Schuller, J. A.; Barnard, E. S.; Cai, W. S.; Jun, Y. C.; White, J. S.; Brongersma, M. L. Plasmonics for Extreme Light Concentration and Manipulation. *Nat. Mater.* **2010**, *9*, 193–204.
4. Naik, G. V.; Shalaev, V. M.; Boltasseva, A. Alternative Plasmonic Materials: Beyond Gold and Silver. *Adv. Mater.* **2013**, *25*, 3264–3294.
5. Naik, G. V.; Boltasseva, A. Semiconductors for Plasmonics and Metamaterials. *Phys. Status Solidi RRL* **2010**, *4*, 295–297.
6. Faucheaux, J. A.; Stanton, A. L. D.; Jain, P. K. Plasmon Resonances of Semiconductor Nanocrystals: Physical Principles and New Opportunities. *J. Phys. Chem. Lett.* **2014**, *5*, 976–985.
7. Pierret, R. F. *Semiconductor Device Fundamentals*; Addison-Wesley: Reading, MA, 1996; p 792.
8. Hessel, C. M.; Pattani, V. P.; Rasch, M.; Panthani, M. G.; Koo, B.; Tunnell, J. W.; Korgel, B. A. Copper Selenide Nanocrystals for Photothermal Therapy. *Nano Lett.* **2011**, *11*, 2560–2566.
9. Llordes, A.; Garcia, G.; Gazquez, J.; Milliron, D. J. Tunable Near-Infrared and Visible-Light Transmittance in Nanocrystal-in-Glass Composites. *Nature* **2013**, *500*, 323–327.
10. Jain, P. K.; Manthiram, K.; Engel, J. H.; White, S. L.; Faucheaux, J. A.; Alivisatos, A. P. Doped Nanocrystals as Plasmonic Probes of Redox Chemistry. *Angew. Chem., Int. Ed.* **2013**, *52*, 13671–13675.
11. Babicheva, V. E.; Kinsey, N.; Naik, G. V.; Ferrera, M.; Lavrinenko, A. V.; Shalaev, V. M.; Boltasseva, A. Towards CMOS-Compatible Nanophotonics: Ultra-Compact Modulators Using Alternative Plasmonic Materials. *Opt. Express* **2013**, *21*, 27326–27337.
12. Tice, D. B.; Li, S. Q.; Tagliazucchi, M.; Buchholz, D. B.; Weiss, E. A.; Chang, R. P. H. Ultrafast Modulation of the Plasma Frequency of Vertically Aligned Indium Tin Oxide Rods. *Nano Lett.* **2014**, *14*, 1120–1126.
13. Maier, S. A.; Brongersma, M. L.; Kik, P. G.; Atwater, H. A. Observation of Near-Field Coupling in Metal Nanoparticle Chains Using Far-Field Polarization Spectroscopy. *Phys. Rev. B* **2002**, *65*, 193408.
14. Sonnichsen, C.; Reinhard, B. M.; Liphardt, J.; Alivisatos, A. P. A Molecular Ruler Based on Plasmon Coupling of Single

Gold and Silver Nanoparticles. *Nat. Biotechnol.* **2005**, *23*, 741–745.
15. Jain, P. K.; Eustis, S.; El-Sayed, M. A. Plasmon Coupling in Nanorod Assemblies: Optical Absorption, Discrete Dipole Approximation Simulation, and Exciton-Coupling Model. *J. Phys. Chem. B* **2006**, *110*, 18243–18253.
16. Halas, N. J.; Lal, S.; Chang, W. S.; Link, S.; Nordlander, P. Plasmons in Strongly Coupled Metallic Nanostructures. *Chem. Rev.* **2011**, *111*, 3913–3961.
17. Willets, K. A.; Van Duyne, R. P. Localized Surface Plasmon Resonance Spectroscopy and Sensing. *Annu. Rev. Phys. Chem.* **2007**, *58*, 267–297.
18. Kauranen, M.; Zayats, A. V. Nonlinear Plasmonics. *Nat. Photonics* **2012**, *6*, 737–748.
19. Kale, M. J.; Avanesian, T.; Christopher, P. Direct Photocatalysis by Plasmonic Nanostructures. *ACS Catal.* **2014**, *4*, 116–128.
20. Jain, P. K.; Huang, W. Y.; El-Sayed, M. A. On the Universal Scaling Behavior of the Distance Decay of Plasmon Coupling in Metal Nanoparticle Pairs: A Plasmon Ruler Equation. *Nano Lett.* **2007**, *7*, 2080–2088.
21. Kodambaka, S.; Tersoff, J.; Reuter, M. C.; Ross, F. M. Diameter-Independent Kinetics in the Vapor-Liquid-Solid Growth of Si Nanowires. *Phys. Rev. Lett.* **2006**, *96*, 096105.
22. Schmidt, V.; Wittemann, J. V.; Gosele, U. Growth, Thermodynamics, and Electrical Properties of Silicon Nanowires. *Chem. Rev.* **2010**, *110*, 361–388.
23. Shi, J.; Wang, X. D. Functional Semiconductor Nanowires *via* Vapor Deposition. *J. Vac. Sci. Technol., B* **2011**, *29*, 060801.
24. Chou, L. W.; Filler, M. A. Engineering Multimodal Localized Surface Plasmon Resonances in Silicon Nanowires. *Angew. Chem., Int. Ed.* **2013**, *52*, 8079–8083.
25. Li, N.; Tan, T. Y.; Gosele, U. Transition Region Width of Nanowire Hetero- and pn-Junctions Grown Using Vapor-Liquid-Solid Processes. *Appl. Phys. A: Mater. Sci. Process.* **2008**, *90*, 591–596.
26. Clark, T. E.; Nimmatoori, P.; Lew, K. K.; Pan, L.; Redwing, J. M.; Dickey, E. C. Diameter Dependent Growth Rate and Interfacial Abruptness in Vapor-Liquid-Solid Si/Si(1-x)Ge(x) Heterostructure Nanowires. *Nano Lett.* **2008**, *8*, 1246–1252.
27. Wen, C. Y.; Reuter, M. C.; Bruley, J.; Tersoff, J.; Kodambaka, S.; Stach, E. A.; Ross, F. M. Formation of Compositionally Abrupt Axial Heterojunctions in Silicon-Germanium Nanowires. *Science* **2009**, *326*, 1247–1250.
28. Perea, D. E.; Li, N.; Dickerson, R. M.; Misra, A.; Picraux, S. T. Controlling Heterojunction Abruptness in VLS-Grown Semiconductor Nanowires *via in Situ* Catalyst Alloying. *Nano Lett.* **2011**, *11*, 3117–3122.
29. Dick, K. A.; Bolinsson, J.; Borg, B. M.; Johansson, J. Controlling the Abruptness of Axial Heterojunctions in III-V Nanowires: Beyond the Reservoir Effect. *Nano Lett.* **2012**, *12*, 3200–3206.
30. Chou, L. W.; Near, R. D.; Boyuk, D. S.; Filler, M. A. Influence of Dielectric Anisotropy on the Absorption Properties of Localized Surface Plasmon Resonances Embedded in Si Nanowires. *J. Phys. Chem. C* **2014**, *118*, 5494–5500.
31. Xie, P.; Hu, Y. J.; Fang, Y.; Huang, J. L.; Lieber, C. M. Diameter-Dependent Dopant Location in Silicon and Germanium Nanowires. *Proc. Natl. Acad. Sci. U.S.A.* **2009**, *106*, 15254–15258.
32. Gan, Z. F.; Perea, D. E.; Yoo, J.; Picraux, S. T.; Smith, D. J.; McCartney, M. R. Mapping Electrostatic Profiles Across Axial p-n Junctions in Si Nanowires Using Off-Axis Electron Holography. *Appl. Phys. Lett.* **2013**, *103*, 153108.
33. Amit, I.; Givan, U.; Connell, J. G.; Paul, D. F.; Hammond, J. S.; Lauhon, L. J.; Rosenwaks, Y. Spatially Resolved Correlation of Active and Total Doping Concentrations in VLS Grown Nanowires. *Nano Lett.* **2013**, *13*, 2598–2604.
34. Koren, E.; Hyun, J. K.; Givan, U.; Hemesath, E. R.; Lauhon, L. J.; Rosenwaks, Y. Obtaining Uniform Dopant Distributions in VLS-Grown Si Nanowires. *Nano Lett.* **2011**, *11*, 183–187.
35. Wei, Q. H.; Su, K. H.; Durant, S.; Zhang, X. Plasmon Resonance of Finite One-Dimensional Au Nanoparticle Chains. *Nano Lett.* **2004**, *4*, 1067–1071.
36. Palik, E. D.; Ghosh, G. *Handbook of Optical Constants of Solids*; Academic Press: San Diego, CA, 1998; p 999.
37. Connell, J. G.; Yoon, K.; Perea, D. E.; Schwalbach, E. J.; Voorhees, P. W.; Lauhon, L. J. Identification of an Intrinsic Source of Doping Inhomogeneity in Vapor-Liquid-Solid-Grown Nanowires. *Nano Lett.* **2013**, *13*, 199–206.
38. Kodambaka, S.; Tersoff, J.; Reuter, M. C.; Ross, F. M. Germanium Nanowire Growth Below the Eutectic Temperature. *Science* **2007**, *316*, 729–732.
39. Christesen, J. D.; Pinion, C. W.; Zhang, X.; McBride, J. R.; Cahoon, J. F. Encoding Abrupt and Uniform Dopant Profiles in Vapor-Liquid-Solid Nanowires by Suppressing the Reservoir Effect of the Liquid Catalyst. *ACS Nano* **2014**, *8*, 11790–8.
40. Mayer, K. M.; Hafner, J. H. Localized Surface Plasmon Resonance Sensors. *Chem. Rev.* **2011**, *111*, 3828–3857.
41. Chou, L. W.; Shin, N.; Sivaram, S. V.; Filler, M. A. Tunable Mid-Infrared Localized Surface Plasmon Resonances in Silicon Nanowires. *J. Am. Chem. Soc.* **2012**, *134*, 16155–16158.
42. Shin, N.; Filler, M. A. Controlling Silicon Nanowire Growth Direction *via* Surface Chemistry. *Nano Lett.* **2012**, *12*, 2865–2870.